Journal of Power Sources 299 (2015) 139–148

Contents lists available at ScienceDirect

Journal of Power Sources

journal homepage: www.elsevier.com/locate/jpowsour

Favorable effect of in-situ generated platinum in the membrane on fuel cell membrane durability

Natalia Macauley [a], Ka Hung Wong [a], Mark Watson [b], Erik Kjeang [a, *]

[a] School of Mechatronic Systems Engineering, Simon Fraser University, 250-13450 102 Avenue, Surrey, BC V3T0A3, Canada
[b] Ballard Power Systems, 9000 Glenlyon Parkway, Burnaby, BC V5J5J8, Canada

HIGHLIGHTS

- Field and lab generated Pt in the membrane (PITM) was analyzed and compared.
- Membrane lifetime enhancement was demonstrated and attributed to the PITM structure.
- High PITM concentration generally correlated with enhanced durability.
- Large interconnected multi-armed Pt particles were most effective.
- Pt dissolution during field operation can assist membrane stability via PITM.

GRAPHICAL ABSTRACT

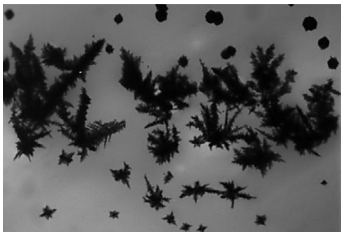

ARTICLE INFO

Article history:
Received 3 July 2015
Received in revised form
25 August 2015
Accepted 26 August 2015
Available online 6 September 2015

Keywords:
Fuel cell
Durability
Membrane
Platinum
Transmission electron microscopy

ABSTRACT

The overall lifetime of polymer electrolyte fuel cells is often determined by the membrane durability. Platinum, which may dissolve from the catalyst layers during fuel cell operation and deposit in the membrane, has been shown to have both positive and negative effects on membrane stability. In the present work, we analyze what specific conditions are required in order to reach a favorable, membrane stabilizing effect with the controlled use of platinum in the membrane. Using accelerated membrane durability testing, field operated membrane samples, and electron microscopy, we demonstrate that a high platinum concentration with specific particle shapes and sizes is essential for enhanced membrane stability. Specifically, star shaped and dendritic particles with high particle density and high surface area are shown to be preferable. These particles contain high levels of Pt(111) and are expected to have high catalytic activity toward peroxide quenching and crossover gas consumption, thereby mitigating chemical membrane degradation. On the other hand, small, dispersed cubic particles are found to have no effect or the opposite, negative effect on membrane stability.

1. Introduction

Polymer electrolyte fuel cells are promising for application in transportation, but automotive driving generates conditions that exacerbate both membrane and catalyst degradation. Heavy and light duty durability targets of 18,000 and 5000 h, respectively [1,2], are yet to be demonstrated in field operation, which makes the development of highly durable fuel cell components a priority. Fuel cell membranes degrade chemically and mechanically during vehicle operation leading to membrane thinning and pinhole and crack formation over time. Chemical membrane degradation occurs primarily due to radical attack of the ionomer, where radicals are

* Corresponding author.
E-mail address: ekjeang@sfu.ca (E. Kjeang).

http://dx.doi.org/10.1016/j.jpowsour.2015.08.096
0378-7753/

mainly produced from hydrogen peroxide in the presence of Fenton's reagents [3–5]. Chemical degradation is most severe at open circuit voltage [6,7] due to a recently proposed iron ion redox cycle that controls the Fe^{2+} concentration in the membrane through reaction-transport phenomena of mobile and redox active iron ions [8]. Mechanical membrane degradation is a result of membrane swelling and shrinking as a response to changes in membrane humidity, eventually leading to membrane fatigue and creep over time [9–12]. Mechanical weakening of membrane properties has also been shown to exacerbate the effect of chemical degradation [12,13]. Mitigation strategies for chemical membrane degradation include chemical stabilization of end groups [14], the use of H_2O_2 decomposition agents such as manganese [15] and zirconia [16], and radical scavengers such as cerium oxide [15,17–19]. Some of the methods used to mitigate mechanical membrane degradation are cross-linking, physical reinforcement with a porous polymer matrix, fibers, or inorganic reinforcement, and ensuring adequate bonding of internal layers [16,20–22].

Fuel cell catalyst layer degradation is caused by Pt dissolution and corrosion of carbon support during fuel cell operation. Pt dissolution occurs during load cycling, when the platinum oxide film that initially forms on the catalyst surface above 0.85 V [23,24] is removed from the catalyst surface once the voltage is swept below 0.6 V [25]. Instability between the Pt–Pt bonds in the first two atomic layers of the catalyst cause Pt ion dissolution and subsequent migration into the membrane [23]. Carbon corrosion is caused by the reverse-current mechanism, which occurs when air is present at the anode and cathode during introduction of hydrogen into the anode upon startup. This results in a high interfacial potential difference in the region where hydrogen is absent. If the potential exceeds 1.1 V, the carbon support in the cathode is electrochemically oxidized into CO_2 [26,27]. Outlets have the highest carbon corrosion levels because incoming hydrogen takes longer to reach them [28]. Carbon corrosion can also occur during localized hydrogen starvation, whereby higher temperatures promote more carbon corrosion [29]. Carbon free supports such as SnO_2 and Ti_4O_7 avoid the issue of carbon corrosion [30].

The chemical reduction of dissolved Pt ions by H_2 permeating through the membrane from the anode side leads to Pt particle deposition in the membrane, and ultimately the formation of a densely packed band at a specific distance from the cathode [31]. The relative local fluxes of H_2 and O_2 within the membrane and the H_2/O_2 partial pressures determine the location of the Pt band [25,32–35], and the incoming crossover gases can be consumed at the Pt band to form water [36]. The potential distribution in the membrane is stepped from 0 V to 0.8–1 V between the anode and cathode, based on H_2 and O_2 permeation in the membrane, respectively [34]. The potential in the vicinity of a Pt particle decreases with increasing particle size in the anodic region and increases in the cathodic region, governing the dominant reaction at each particle surface [37]. In general, Pt particles can take a wide variety of shapes and sizes, and the most common shapes include truncated nanooctahedrons, nanocubes, and nanooctapods [38]. About 80% of the total surface area of Pt nanoparticles is composed of face centered cubic (fcc) (111) faces [39]. Pt nanocrystals exhibit shape- and size-dependent catalytic properties [39]. Tetrahedral nanoparticles have the highest fraction of surface atoms located on corners and edges [40] and consist of mostly Pt(111), which has the most stable close-packed surfaces and the lowest activation energy [38]. Thereby, the catalytic activity of Pt surfaces identified in tetrahedral, spherical, and cubic particles follows the order of Pt(111) > Pt(411) > Pt(100), respectively [38].

In regards to the chemical stability of the membrane, both positive and negative effects of platinum in the membrane (PITM) have been reported. The preparation method of membranes with Pt seems to influence the membrane response. For instance, ion-exchange with platinum-complex ions in $[Pt(NH_3)_4]Cl_2$ solution followed by reduction in 1-pentanol resulted in a reduced fluoride emission in durability tests [41]. On the other hand, co-casting of PFSA membranes with Pt particles led to poor mechanical integrity, where the presence of Pt in the membrane was reported to increase membrane degradation due to increased radical formation [42–49]. Higher levels of OH radical formation at Pt particles in the membrane were detected at the anode side [50]. Helmly et al. examined chemically degraded membranes by atomic force microscopy and found the formation of electronic short-circuits due to the accumulation of Pt particles in the membrane, which led to enhanced degradation via formation of peroxide radicals and significant heat generation [45]. Rodgers et al. also attributed membrane degradation to Pt band formation in the membrane [46], but later concluded that high densities of PITM may deactivate generated radicals before they can attack the ionomer [43,44]. Helmly et al. did not identify degradation in membranes with Pt formed in-situ, which however was seen in membranes with ex-situ impregnated Pt [47]. Meanwhile, hydrogen peroxide and hydroxyl radical scavenging abilities of Pt nanoparticles have been shown ex-situ [51–56] and the mitigating effect of the Pt band toward chemical degradation was demonstrated in-situ in our previous work [57,58]. 2800 h field operated samples showed enhanced durability under accelerated stress test conditions [56] due to the presence of a naturally formed Pt band in the membrane. Further investigations were conducted by simulating specific duty cycle operating conditions in order to replicate the PITM formation process in the lab, and then subjecting the membranes with artificially deposited PITM to an accelerated membrane durability test (AMDT) [57], in which they too displayed visible lifetime extensions. In sharp contrast to regular membranes, membranes with PITM showed no membrane thinning, low fluoride emission rates, and highly preserved mechanical strength [58], meaning that the PITM must have substantially reduced the chemical degradation, presumably by decomposing H_2O_2 to non-radical products [56,59] and/or converting crossover gases to water. However, the opposing results in the literature make the study of Pt particles in membranes with both enhanced and reduced durability important in order to understand the underlying mechanisms. Other methods of nanoparticle synthesis and incorporation into the membrane include scanning probe block copolymer lithography [60–62] and electrochemical atomic layer deposition [63,64].

The objective of the present work is to identify the main differences between Pt particles in the membrane responsible for increased membrane stability and those that increase membrane degradation. Therefore, the effect of various PITM concentrations on membrane durability is first evaluated under AMDT conditions. The distribution and structure of the Pt particles in the laboratory generated PITM are then compared to the corresponding Pt particles observed in field operated membranes using transmission electron microscopy [65]. Finally, the Pt particle size, shape, and density in the various membranes are correlated to membrane stability, with the intention of elucidating the underlying mechanism of enhanced stability by the Pt band [57,58].

2. Experimental

Pt was first dissolved into the membrane from the cathode catalyst layer using a confidential in-situ protocol developed by Ballard Power Systems, which simulates processes responsible for Pt migration into the membrane during duty cycle operation. Membranes with laboratory generated Pt band were degraded under accelerated membrane durability test (AMDT) conditions. Membrane electrode assemblies (MEAs) used for the AMDT were

made of catalyzed gas diffusion electrodes (GDEs). The GDEs were fabricated by coating a micro-porous layer made of polytetrafluorethylene (PTFE) and carbon black on a non-woven carbon paper gas diffusion layer substrate [66] followed by coating of a catalyst layer that consisted of carbon-supported platinum catalyst and perfluorosulfonic acid (PFSA) ionomer [66]. MEAs were prepared by hot-pressing a standard non-reinforced PFSA ionomer membrane with anode and cathode GDEs [66].

The MEAs were tested in-situ using a 10-cell stack subjected to the recently developed AMDT protocol for heavy duty fuel cells with combined chemical and mechanical degradation [58]. The baseline AMDT was designed to estimate membrane durability by simulating the most stressful conditions for the membrane during bus driving, which includes idling at high voltages and hygro-thermal variations due to the dynamic power demand from the vehicle. Therefore, a voltage hold at 9 V was applied to induce chemical degradation combined with mechanical stress from relative humidity (RH) cycling [58]. To further accelerate membrane degradation, the temperature and oxygen partial pressure were elevated to 85 °C and 45%, respectively. An in-house technique was used to dissolve Pt from the cathode catalyst layer, allowing it to migrate into the membrane. Four variants of this technique were used to apply PITM either before or during AMDT operation. In the first case, 1000 PITM generating cycles were applied prior to exposing the membrane to baseline AMDT conditions, denoted as LAB1. In the second case, one PITM generating cycle was integrated into the AMDT protocol after every 6th RH cycle, denoted as LAB2. LAB3 integrated a PITM generating cycle after every 12th RH cycle of the AMDT protocol, in this case using air conditions (21% O_2 concentration). Finally, LAB4 integrated a PITM generating cycle after every 24th RH cycle. All stacks with applied PITM were operated until failure as defined by the threshold hydrogen leak rate across the membrane of 100 sccm. Effluent water was collected from the stack for fluoride emission rate (FER) determination before regular leak tests, after which a polarization curve was measured.

At the end of the test, an infrared (IR) camera was used to find the distribution of membrane leaks. Membrane thickness was measured using cross-sectional scanning electron microscopy (SEM; JEOL JSM-6360). The Pt concentration in the Pt band was measured by energy-dispersive X-ray spectroscopy (EDS) elemental analysis on the SEM. Transmission electron microscopy (TEM) was used to analyze the distribution and structure of the Pt particles in the membranes. TEM sample preparation was done on MEAs dried at ambient conditions for two hours prior to cutting out 1 cm^2 sections from the MEA inlet, middle, and outlet regions. The sections were further cut diagonally into identical triangles to create a tip. GDLs were carefully peeled off and the remaining catalyst coated membranes (CCMs) were embedded in Araldite 502 epoxy and cured at 70 °C for 12 h. A LEICA ultra-microtome was used to cut the embedded CCMs into 80–100 nm thin slices, always using a freshly prepared glass knife. Slices were placed on formvar coated 200-mesh copper grids, model FF200-Cu. Two transmission electron microscopes, STEM Hitachi-8100 and STEM FEI Tecnai Osiris, were used for nano-imaging of the Pt particles in the membrane at 200 kV. Image processing was done in ImageJ.

Field operated membrane samples were cut from partially aged MEAs extracted from the Whistler, British Columbia fuel cell bus fleet after 2,800, 4400 and 8200 h of field operation. The real-world duty cycle experienced by these MEAs was similar albeit milder in nature to the conditions of the AMDT, featuring both chemical and mechanical membrane degradation. Additionally, as a result of catalyst layer degradation, these MEAs developed a Pt band in the membrane during regular bus operation. Field operated membranes were also leak tested to detect leaks and IR imaging was used to locate the position of leaks. Membrane thickness was identified by SEM and EDS was used to measure the Pt concentration of the Pt band. Finally, TEM was used to analyze the Pt particle structure and distribution in the membranes.

3. Results and discussion

To simulate the stabilizing effect of the Pt band seen in field operated membranes, membranes with laboratory generated platinum bands were produced in-situ and the effect of PITM on membrane stability was investigated under baseline AMDT conditions. As a reference, freshly manufactured membranes without PITM were exposed to baseline AMDT conditions at 21% and 45% O_2. Four different variations of laboratory generated PITM were introduced by changing the frequency of the PITM generating cycles and their combination with the AMDT protocol. Firstly, a Pt band was generated prior to exposure to AMDT conditions in LAB1 to support the assumption that at mild operating conditions, membrane degradation may be negligible prior to Pt band formation in the field. On the other hand, integrating PITM generating cycles into the AMDT in LAB2, LAB3, and LAB4 after every 6th, 12th, and 24th RH cycle, respectively, may better simulate the real condition. In this case, the assumption is that Pt band generation in the field is gradual, and the membrane is exposed to degrading conditions prior to and during Pt band formation. To determine which mechanism is more plausible, the structure and distribution of laboratory generated Pt nanoparticles in the membrane was compared with PITM generated under field operating conditions. The findings were correlated to mitigation of chemical membrane degradation.

The membrane leak rate development was monitored during the AMDT as an indicator of membrane health, as shown in Fig. 1. The stack failure threshold was a leak rate of 100 sccm (10 sccm per cell). The lifetime of membranes with laboratory generated PITM was compared to the lifetime of reference membranes. The reference membrane lifetime was 298 h, and all ten cells failed with leak rates above 10 sccm [58]. LAB1 membranes displayed extended lifetime compared to the reference membranes, and lasted 435 h, with half of the cells in the stack still healthy. The Pt particles in LAB1, which were generated in the membrane prior to degradation, thereby successfully extended the membrane lifetime by approximately 50%. In LAB2, PITM was gradually deposited in the membrane by integrating a single PITM generating cycle after every 6th RH cycle of the baseline AMDT. LAB2 membranes displayed ~130% lifetime extension compared to reference membranes, by lasting 692 h. In addition, only two out of ten membranes actually failed with a leak rate above 10 sccm, which is supported by the slow leak

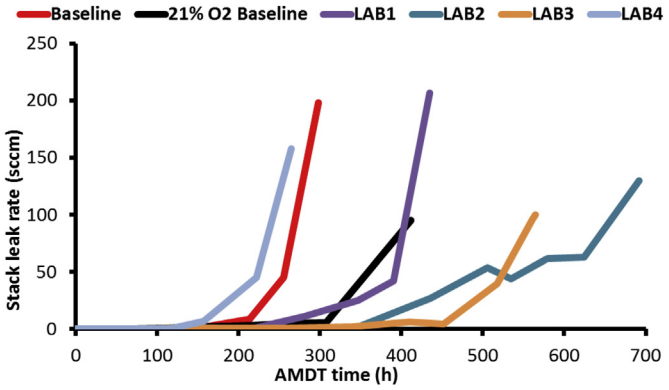

Fig. 1. AMDT stack leak rate development with reference (regular AMDT baseline and 21% O_2 baseline) and Pt containing (LAB1, LAB2, LAB3, and LAB4) membranes.

rate growth indicating local rather than global failure. A lower PITM concentration was generated in LAB3 by using a PITM generating cycle after every 12th RH cycle in a modified AMDT using air as oxidant, i.e., less frequently compared to LAB2. Despite the lower PITM loading, LAB3 still surpassed the lifetime of reference membranes at air conditions (412 h; seven failed membranes) with a lifetime of 564 h and only two failed membranes. This is evidence that LAB3 still contained sufficient PITM to preserve a higher number of membranes in the stack for a longer time, with a ~40% stack lifetime extension compared to the reference. Lastly, LAB4 was designed to have the lowest amount of PITM by using a PITM generating cycle after every 24th RH cycle of the baseline AMDT (at 45% O_2). In this case, the lifetime of the membranes in LAB4 was shorter than the baseline, lasting only 243 h, with eight failed membranes. The low lifetime (~20% *below* the reference) and high number of failed membranes in LAB4 indicates a much less effective Pt band compared to the previous membranes with PITM. As a result of PITM, LAB1, LAB2, and LAB3 lasted 50%, 130%, and 40% longer than the reference stacks, respectively. LAB4 on the other hand had a lower lifetime than the reference, presumably due to the low PITM concentration.

Fig. 2 compares the Pt concentration at the Pt band location of the AMDT operated membranes (LAB1-4) to those of the field operated membranes (FOMs) obtained from the Whistler, British Columbia fuel cell bus fleet. As a result of the 21% O_2 partial pressure in air, the Pt band was identified 20% away from the cathode interface in FOMs and LAB3 membranes. Similarly, the Pt band in the LAB1, LAB2, and LAB4 membranes was located 33%–40% away from the cathode due to the elevated 45% O_2 partial pressure. The Pt concentration was observed to increase from MEA inlet to outlet in all cases for both AMDT and field operated membranes. During extended field operation the outlet Pt concentration of the FOMs gradually increased from 3700 to 5700 ppm between 2800 and 8200 h of operation. The higher operating temperature of the AMDT operated membranes resulted in increased catalyst dissolution, especially in regions near the MEA outlets, where Pt concentrations reached 10,000–40,000 ppm. The Pt band concentration in the LAB1 membranes was relatively close to that of the FOMs, indicating a realistic amount of PITM. The integrated PITM generating protocol used in LAB2-4 is however believed to better represent the situation in the field, since Pt gradually migrates from the cathode into the membrane during field operation (unlike LAB1). LAB2 membranes accumulated significantly more PITM than LAB1, which was reflected in a much longer AMDT lifetime. LAB3 and LAB4 were used to generate PITM concentrations closer to the FOMs by reducing the frequency of the PITM generating cycles during the AMDT operation. However, the LAB3 membranes still contained substantially more Pt than the FOMs, while the LAB4 membranes contained less Pt at the inlet and more Pt at the outlet compared to the FOMs. As mentioned previously, there was a positive effect on membrane stability in LAB3, while LAB4 had a negative effect. Consequently, although the Pt band was generally favorable for membrane stability, there was no direct correlation between PITM concentration and membrane lifetime. Furthermore, it is noteworthy that LAB1 had a lower PITM concentration than LAB4 but still achieved a 40% increase in lifetime, presumably due to the pre-AMDT application of the Pt band.

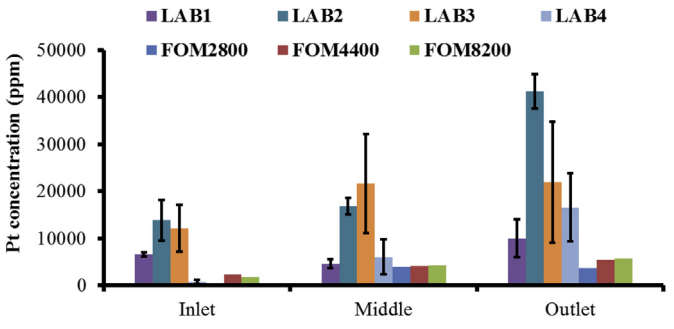

Fig. 2. Pt concentration at the Pt band location of the AMDT (LAB1-4) and field operated (FOM) membranes measured at three regions from MEA inlet to outlet.

3.1. Pt particle shapes

The Pt particle structure may also contribute to the membrane stability effects associated with PITM. For this reason, the Pt particle shapes across the thickness of the membrane were analyzed by TEM, focusing on the membrane region close to the MEA outlet which had the highest Pt concentration. Fig. 3 shows typical images of Pt particles identified in the FOMs from the areas close to the anode, middle, and near the cathode where the Pt band was located. The 2800 h FOMs (Fig. 3a–c) contained a mix of spherical, cubic, and triangular particles with smooth surfaces throughout the membrane. In addition, curly dendritic particles were present close to the cathode, at the location of the Pt band. Smooth tetrahedral and cubic particles populated the middle of the 4400 h FOMs along with tripod and star shaped particles (Fig. 3e). The curly dendritic particles close to the cathode grew in size over time, likely due to agglomeration of smaller particles, while small cubic particles occupied the narrow space between the cathode and the Pt band (Fig. 3f). A distinct transition to star shaped particles was observed in the middle of the 8200 h FOMs (Fig. 3h). Close to the cathode (Fig. 3i), growth of curly dendritic particles was observed across the entire space, with no sign of cubic particles. The area near the anode was sparsely populated with seed particles, i.e., smooth tiny spherical or cubic particles, with no significant changes over time.

Fig. 4 shows the Pt particle distribution in the AMDT operated membranes (LAB1-4) with laboratory generated PITM. Similar to the FOMs, the anode region contained unremarkable small spherical or cubic particles in all cases. A combination of smooth cubic, tetrahedral, star, and diamond shaped particles appeared in the middle of the LAB1 membranes (Fig. 4b), while curly dendritic particles were observed close to the cathode (Fig. 4c), similar to those identified in the FOMs. These particles are a confirmation of successful laboratory replication of the field generated PITM distribution and particle shapes, in particular at the critical location of the Pt band. Due to the high amount of PITM, the particles in LAB2 formed more complex shapes at the Pt band (Fig. 4f) compared to LAB1. Star shaped particles in the middle (Fig. 4e) gradually transformed into large highly branched interconnected multi-armed particles with very sharp surfaces at the Pt band (Fig. 4f), which may have been responsible for the longer lifetime of LAB2 compared to LAB1. Additionally, large smooth cubic particles occupied the space between the Pt band and the cathode. The middle of the LAB3 membranes contained tripod and star shaped particles (Fig. 4h), and the Pt band was formed by interconnected dendritic particles with sharp surfaces (Fig. 4i), similar to those in LAB2 albeit less complex, along with occasional smooth cubic particles. In stark contrast, LAB4 membranes (Fig. 4j–l) were dominated by a single particle shape: cubic particles, gradually increasing in size from the middle to the cathode. LAB4 had somewhat lower AMDT lifetime than the baseline without PITM, suggesting that the cubic particles had no effect, or possibly a slightly negative effect, on the membrane lifetime. Some cubic particles close to the cathode were in initial stages of expansion, with tiny spikes forming in the corners. This indicates that the more complex particles observed in LAB2 and LAB3 were also initially cubic. In general, particle shape complexity increased from anode

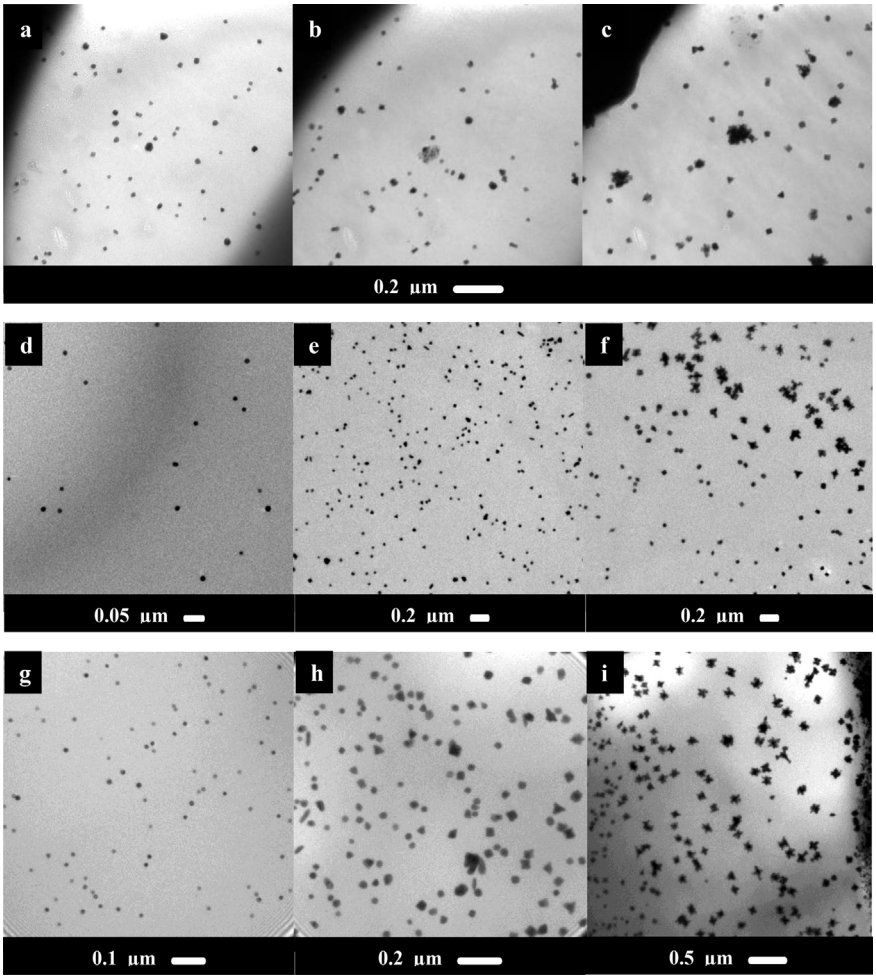

Fig. 3. PITM from anode (left) to cathode (right) in field operated membranes at a–c) 2800 h, d–f) 4400 h, and g–i) 8200 h.

to cathode, and the Pt band region near the cathode featured a variety of smooth, curly, and spiky dendritic particles in all cases except for LAB4. Furthermore, all membranes had spherical and cubic particles in common. The surface area of Pt nanoparticles is known to influence catalytic activity [67], i.e., rough surfaces have higher catalytic activity due to higher surface area and a higher number of kinks and edges exposed to reactions, which could be favorable for membrane stability. The roughest particle surfaces were observed on particles within the Pt band and close to the cathode.

3.2. Pt particle size distribution

Since the Pt particles had various shapes, the average particle diameter was selected as the primary particle size metric. As shown in Fig. 5, the average Pt particle size as well as the particle size variability gradually increased from anode to cathode, with a peak at the Pt band region. Most particles were below 200 nm in diameter except for the large dendritic particles observed at the band. The largest particles detected in the FOMs grew over time from ~90 nm at 2800 h to ~180 nm at 4400 h followed by a marginal growth to ~190 nm at 8200 h. The particle sizes in the AMDT operated membranes were generally larger than those in the FOMs. However, the particle sizes of the LAB1 membranes were very similar to those of the FOMs, in agreement with the similar Pt concentration, particle shapes, and distribution previously noted, again confirming the realistic PITM features of LAB1. The high PITM concentration in LAB2 allowed for the formation of up to ~2 μm interconnected multi-armed particles and ~350 nm cubic particles near the cathode. The highly branched particles in the Pt band of the LAB3 membranes exceeded 1 μm, and the cubic particles typical to LAB4 membranes were up to ~350 nm in size. Small particles are known to have a high surface area and therefore high catalytic activity, while large dendritic particles may also attain high surface area due to their high surface roughness. In contrast, the large cubic particles of LAB4 would have relatively low surface area per unit Pt.

3.3. Pt particle volumetric density and average inter-particle distance

Fig. 6 presents the Pt particle volumetric density at selected regions across the membrane from anode to cathode. The particle volumetric density is given as the number of Pt particles detected per μm^3 of membrane volume; considering a membrane depth equal to the thickness of the ultra-microtomed membrane sections. In addition, the average inter-particle distance in the 2D view of the TEM images is shown in Fig. 7. The seed particle density was generally higher in the anode and middle regions than in the cathode region of the membranes. Due to the appearance of large dendritic particles toward the cathode, the particle density tended to drop while the inter-particle distance increased, coinciding with the Pt band. The particle density decreased over time in the

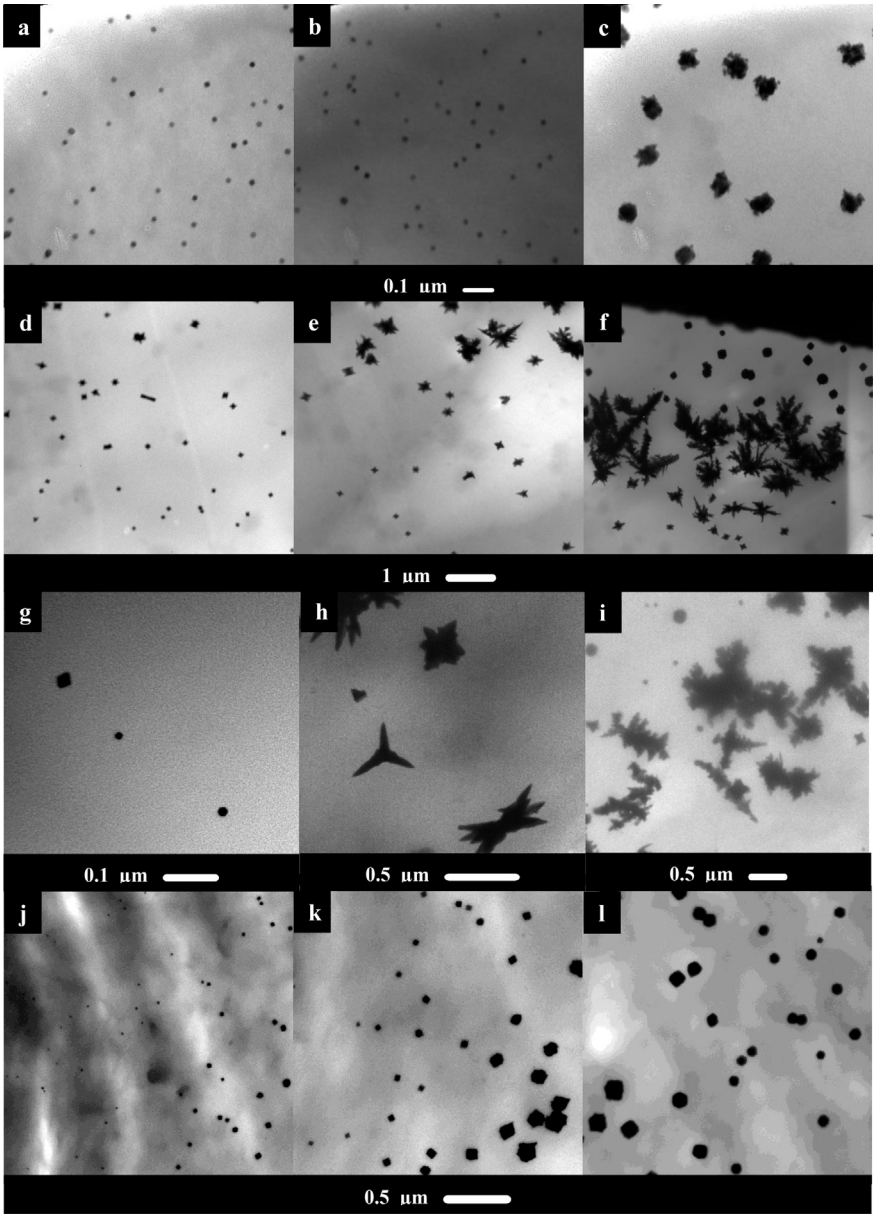

Fig. 4. PITM from anode (left) to cathode (right) in AMDT operated membranes with laboratory generated PITM: a–c) LAB1; d–f) LAB2; g–i) LAB3; and j–l) LAB4.

cathodic region of the FOMs due to a gradual change in particle population from a high number of small particles to a low number of large particles. Considering that the overall Pt concentration was relatively constant, this suggests that Pt particles were agglomerating over time. Moreover, a significant increase in particle density was observed in the anodic region after 8200 h of field operation, indicating that Pt migrated deeper into the membrane over time. These particles were the closest packed group observed in this work.

The highest density of Pt particles in the AMDT operated membranes was generally found in the middle while the highest inter-particle distance was near the cathode. LAB1 had very similar volumetric density and inter-particle spacing to the FOMs, in agreement with the previously observed metrics. LAB2 exhibited the lowest volumetric density and highest inter-particle distance, which correlates to the high Pt concentration and large particle size compared to the other membranes. LAB3 and LAB4 also had much lower particle densities than LAB1 and the FOMs with higher inter-particle distances.

3.4. Lattice fringe analysis

The facets on the surface of the Pt particles can provide additional information about the affinity toward reactions that either mitigate or promote membrane degradation. In order to identify the crystal structure of the Pt particles in the membranes, the distance between certain crystal planes, i.e., *d*-spacings, was measured from fast Fourier transform (FFT) images obtained with high resolution TEM (HRTEM). Dendritic Pt particles, such as those observed in the FOMs and LAB1-3 membranes, are known to contain highly catalytically active (111) facets with typical *d*-spacings of 0.23 nm [68], which are therefore expected to facilitate reactive sites inside the membrane. Due to their abundance in the membrane, lattice fringes of a star shaped particle were analyzed. Fig. 8a shows a typical 50 nm star shaped particle from the middle of the 4400 h FOM. Lattice fringes from the edge of the star are

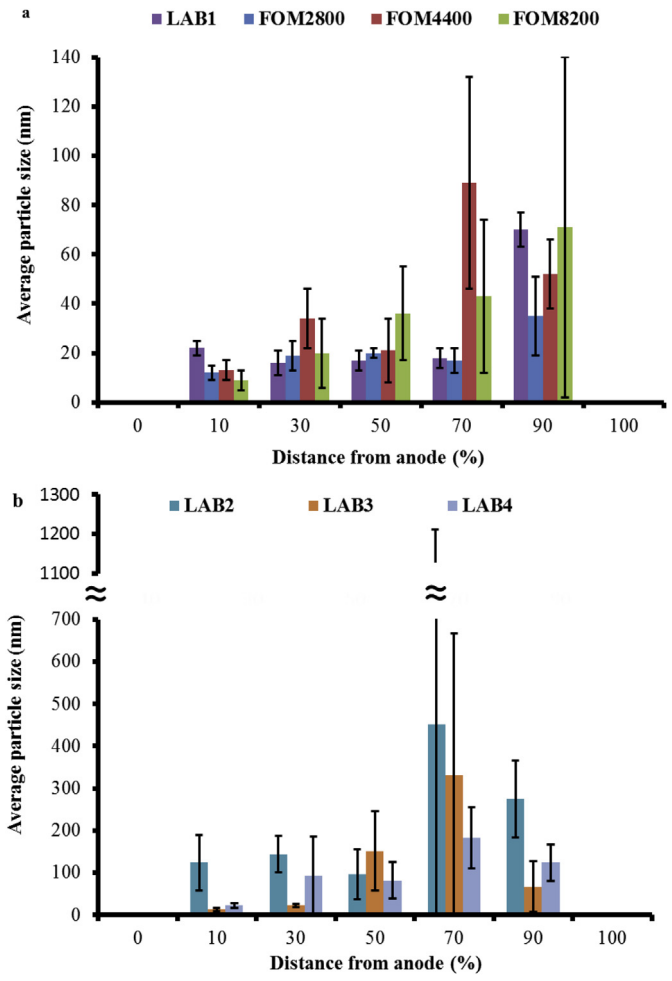

Fig. 5. Pt particle size distribution across the membrane from anode to cathode in: a) LAB1, FOM2800, FOM4400, and FOM8200; and b) LAB2, LAB3, and LAB4.

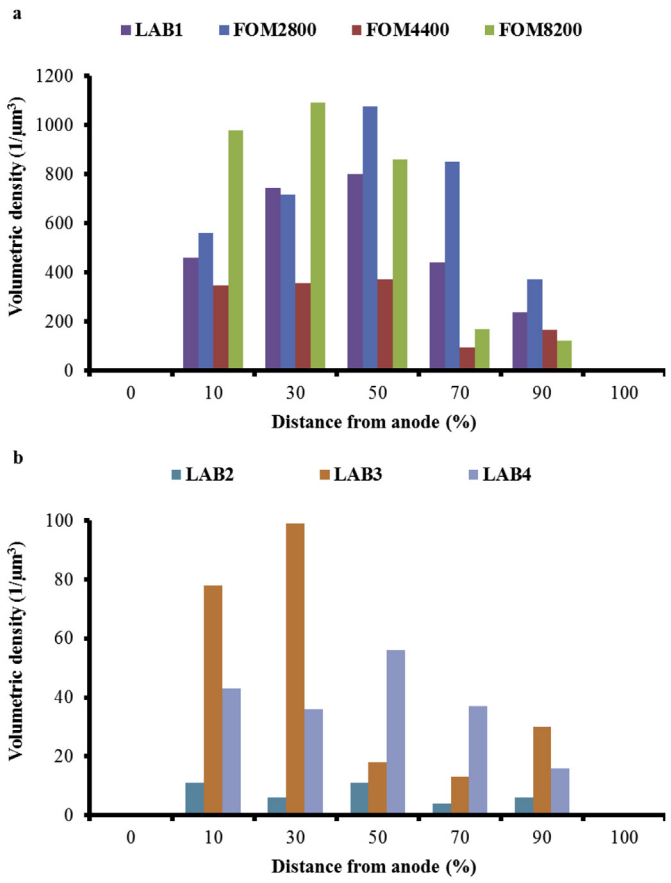

Fig. 6. Volumetric density of Pt particles across the membrane from anode to cathode in: a) LAB1, FOM2800, FOM4400, and FOM8200; and b) LAB2, LAB3, and LAB4.

observed in Fig. 8b. The FFT image from Box 1 in Fig. 8b is shown in Fig. 8c, where the pattern confirms the presence of a face-centered cubic phase, where the interplanar *d*-spacing of 0.23 nm was identified, which corresponds to (111) *hkl* facet of Pt. Additionally, Fig. 8d shows the FFT image of Box 2, where a *d*-spacing of 0.23 nm was also identified, showing the presence of the same (111) lattice plane. However, this region also contains 0.20 and 0.37 nm *d*-spacings, which can be assigned to (200) and (100) lattice planes, respectively.

4. Discussion

The hypothesis that PITM has a positive effect on membrane durability was first established when 2800 h FOMs displayed enhanced membrane durability under highly aggressive accelerated stress test conditions due to the presence of a Pt band in the membrane [57]. For further investigation, membranes with four different PITM formulations (LAB1-4) were subjected to less aggressive AMDT conditions, which are more representative of field conditions [58]. LAB1, LAB2, and LAB3 surpassed the regular membrane durability, while LAB4, which had the lowest frequency of PITM generating cycles, did not. This led to the initial presumption that high PITM concentration leads to higher membrane durability under AMDT conditions. However, the PITM concentrations of LAB1 and LAB4 were roughly the same despite a significant difference in AMDT lifetime, which indicates that other features of PITM may also be important. Most notably, all membranes in LAB1-3 contained large dendritic Pt particles at the critical location of the Pt band, while the membranes in LAB4 merely exhibited cubic particles.

The Pt particle shape is controlled by minimization of surface energy and interfacial kinetics of Pt reduction and subsequent Pt atomic incorporation onto different Pt surfaces. The equilibrium shape of a Pt crystal at zero temperature is a truncated octahedron

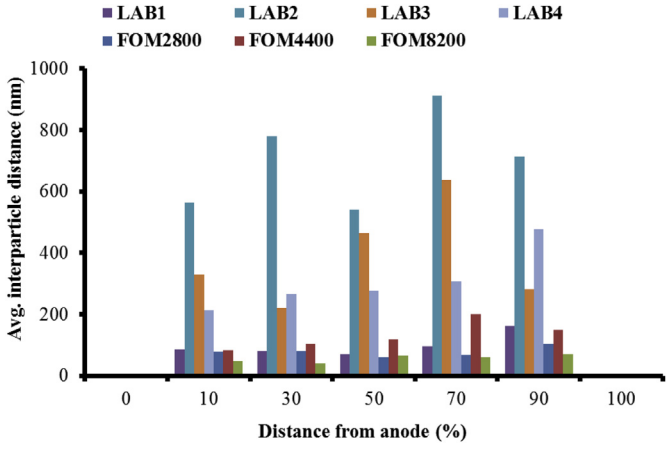

Fig. 7. Average inter-particle distance in the AMDT (LAB1-4) and field operated membranes (FOM2800-8200).

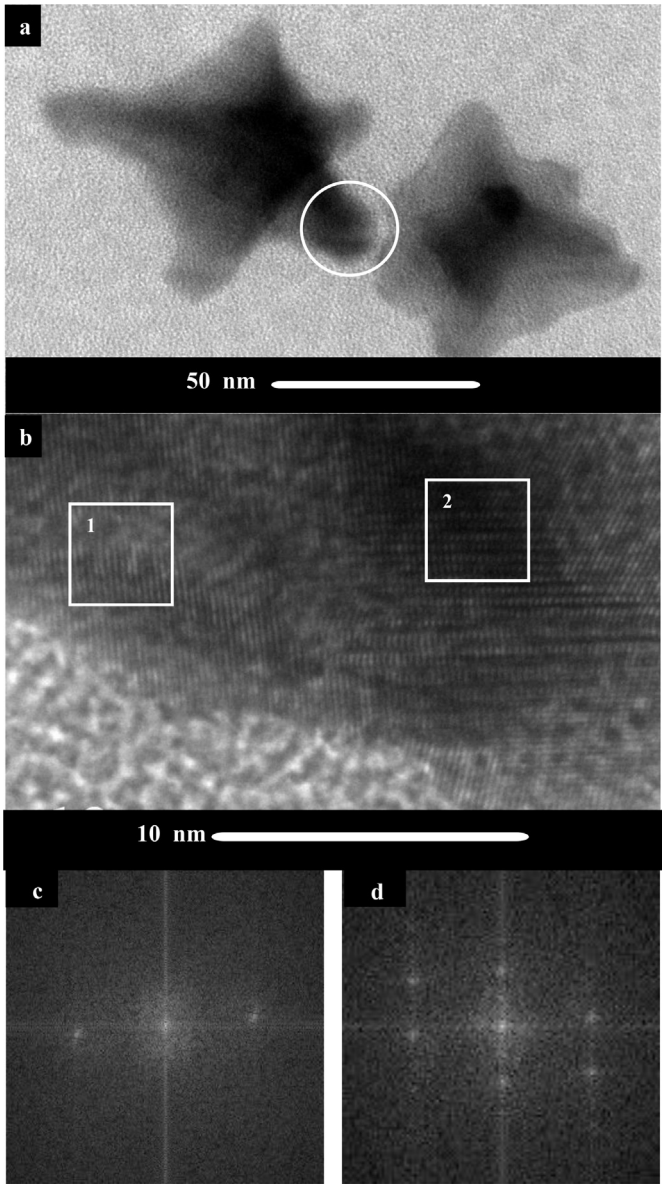

Fig. 8. Detailed analysis of a star shaped particle in the 4400 h field operated membrane (FOM4400): a) particle geometry; b) lattice fringes; and c–d) fast Fourier transform (FFT) images of Boxes 1 and 2 in b), respectively.

consisting predominantly of (111) and (100) facets, which transforms into a truncated square cuboid shape in the presence of H_2 [69]. The formation of different faceted shapes is a result of the difference in partial pressure of H_2 adjacent to the Pt nuclei, which varies throughout the depth of the membrane. The smallest particles observed here were faceted spheres, triangles, cubes, and diamond-shaped structures. The transition from faceted to dendritic growth of Pt nanocrystals depends on the interfacial kinetics for reduction of Pt ions as well as the local concentrations of Pt ions and H_2 [70]. More complex star-shaped particles were generated in the region between the middle of the membrane and the Pt band. Multiarmed nanostars with single-crystal nanostructure are known to grow along (111) facets from tetrahedral particles [71] and exhibit improved electro-catalytic activity and stability due to favorable surface exposure for catalytic reactions [72]. The presence of Pt(111) and Pt(200) was confirmed in the star-shaped particle located in the middle of the 4400 h field operated membrane. These are positive findings for membrane stability, since the anodic region is otherwise favorable for hydrogen peroxide formation. Furthermore, such particles can contribute to water production inside the membrane, leading to improved membrane hydration. The curly dendritic particles observed at the Pt band of all membranes except LAB4 have been reported to contain Pt(111) facets with high catalytic activity [68], which could provide effective sites for quenching of H_2O_2 and crossover gases. Hence, due to the presence of curly dendritic Pt particles, the FOMs are expected to be more stable than LAB4 despite the lower PITM concentration. Such particles are expected to have higher surface area than the cubic particles in LAB4, which were ineffective in membrane lifetime extension. Cubic particles are likely an initial stage of the more mature tree-like structures, and are known to contain mainly Pt(100) facets with lower catalytic activity than Pt(111) [73]. Pt particles grown in regions with high Pt ion availability formed complex tree-like structures such as those in LAB2 and LAB3 membranes. Their rough surfaces, indicative of a high surface area, were effective in extending membrane life, presumably due to favorable kinetics for hydrogen peroxide quenching and gas crossover elimination.

In order to verify this theory, the rate of H_2O_2 quenching into water and oxygen in the presence of PITM was estimated by numerical simulations. The average concentration of H_2O_2 in the membrane under AMDT conditions was calculated using the method described in Wong et al. [8,74]. H_2O_2 formation from crossover oxygen at the anode and from the ORR at the cathode was taken into account and the average H_2O_2 concentration in the membrane was estimated to be 0.15 mol m^{-3}. For simplicity, a Gaussian distribution was applied to the Pt particles in the membrane, where the Pt band thickness was used as the peak width. The variation in Pt band thickness from MEA inlet to outlet was measured by SEM and is shown in Table 1. The kinetics of H_2O_2 quenching by Pt nanoparticles were estimated to be 0.0257 m^3 mol^{-1} s^{-1}, based on information provided by Shiraishi et al. [59]. The average quenching rate of the Pt particles in LAB1 and LAB2 was then calculated based on the Pt concentration and the initial membrane H_2O_2 concentration of 0.15 mol m^{-3}. The source term used to calculate the H_2O_2 quenching rate was:

$$r_{H2O2\ \ quench} = kc_{Pt}c_{H2O2} \quad (1)$$

where k represents the kinetics, c_{Pt} is the Pt concentration in the band, and c_{H2O2} is the hydrogen peroxide concentration. It is important to note that the quenching rate depends on both Pt band concentration and thickness. The average amount of residual H_2O_2 is shown in Table 2, whereby it is estimated that 74–85% and 93–97% of H_2O_2 can potentially be quenched in LAB1 and LAB2, respectively, which is in good agreement with the corresponding durability enhancements. Due to the similarities of the Pt particles between LAB1 and the FOMs, similar results can be expected during field operation. The amount of radicals formed on the Pt particles was however not considered in this calculation, but it is assumed that for all membranes with enhanced durability (LAB1-3 and FOMs), peroxide quenching is more prevalent than radical formation on the PITM. Reduction of the H_2O_2 formation rate at the anode

Table 1
Average Pt band thickness in LAB1 and LAB2 membranes.

	Pt band thickness (μm)		
	Inlet	Middle	Outlet
LAB1	2.95	4.15	2.85
LAB2	3.9	3.45	7.35

Table 2
Residual hydrogen peroxide concentration in the membrane.

	Residual H_2O_2 concentration (mol m^{-3})		
	Inlet	Middle	Outlet
LAB1	0.0388	0.0334	0.0229
LAB2	0.00870	0.00990	0.0041

could also be achieved by reducing oxygen crossover to water at Pt particles in the membrane [75], and given the location of the Pt band at the intersection of the H_2 and O_2 fluxes, the large interconnected particles in the Pt band are likely to form a considerable barrier for crossover gases compared to the more dispersed, small cubic particles. Quenching of hydrogen peroxide and the reduction of crossover gases are therefore the principal mechanisms attributed to enhanced membrane stability. In conclusion, not only the PITM concentration, but the presence of PITM with the right shape and facet, i.e. large Pt(111) faceted dendritic particles at the Pt band location, is relevant to enhancement of membrane stability. The AMDT results for LAB1 indicate that a ~50% lifetime improvement is possible based on the PITM levels observed in field operated membranes.

5. Conclusions

Pt particle shapes, sizes, and distribution in the membrane was analyzed in field and laboratory operated membranes and the findings were correlated to membrane lifetime. Since the total PITM concentration in the field operated membranes was relatively constant over time, smaller particles were observed to gradually agglomerate to form larger particles. The Pt particle structure observed in these membranes was successfully reproduced in the laboratory, and enhanced durability of membranes with curly dendritic particles at the Pt band location was confirmed under AMDT conditions. Laboratory operated membranes with large interconnected tree-like structures, curly dendritic, and star-shaped particles also displayed enhanced durability due to high Pt(111) content and high surface area, leading to high catalytic activity toward peroxide quenching and crossover gas consumption. On the other hand, small cubic particles had no apparent durability enhancing effect. In the former case, it was estimated that 74–97% of H_2O_2 can potentially be quenched in the presence of PITM. Such significant H_2O_2 removal and the anticipated conversion of crossover gases into water are expected to result in mitigation of chemical membrane degradation during fuel cell operation. Thus, catalyst dissolution during field operation can have a positive impact on membrane durability due to the PITM formed.

Acknowledgments

Funding for this research was provided by Automotive Partnership Canada (APC) and the Natural Sciences and Engineering Research Council of Canada (NSERC). Materials and testing facilities were provided by Ballard Power Systems. The Holdcroft Group at SFU is acknowledged for the use of the ultra-microtome. We thank Mark Cruickshank, Curtis Allen, and Joanna Kolodziej for their contributions to testing and failure analysis. We also acknowledge 4D LABS for TEM usage and prompt technical support by Xin Zhang.

References

[1] U.S. DRIVE Partnership, Fuel Cell Technical Team Roadmap, 2013. http://energy.gov/sites/prod/files/2014/02/f8/fctt_roadmap_june2013.pdf.
[2] U.S. DOE National Renewable Energy Laboratory, Fuel Cell Buses in U.S. Transit Fleets: Current Status, 2012. http://www.energy.gov/sites/prod/files/2014/03/f12/fceb_status_2012.pdf.
[3] L. Ghassemzadeh, K. Kreuer, J. Phys. Chem. C (2010) 14635–14645.
[4] L. Ghassemzadeh, T.J. Peckham, T. Weissbach, X. Luo, S. Holdcroft, J. Am. Chem. Soc. 135 (2013) 15923–15932.
[5] L. Ghassemzadeh, S. Holdcroft, J. Am. Chem. Soc. 135 (2013) 8181–8184.
[6] A. Ohma, S. Yamamoto, K. Shinohara, J. Power Sources 182 (2008) 39–47.
[7] A. Ohma, S. Suga, S. Yamamoto, K. Shinohara, J. Electrochem. Soc. 154 (2007) B757.
[8] K.H. Wong, E. Kjeang, ChemSusChem 8 (2015) 1072–1082.
[9] R.M.H. Khorasany, E. Kjeang, G.G. Wang, R.K.N.D. Rajapakse, J. Power Sources 279 (2015) 55–63.
[10] R.M.H. Khorasany, A. Sadeghi Alavijeh, E. Kjeang, G.G. Wang, R.K.N.D. Rajapakse, J. Power Sources 274 (2015) 1208–1216.
[11] M.B. Satterfield, J.B. Benziger, J. Polym. Sci. Part B Polym. Phys. (2008) 11–24.
[12] A. Sadeghi Alavijeh, M.-A. Goulet, R.M.H. Khorasany, J. Ghataurah, C. Lim, M. Lauritzen, E. Kjeang, G.G. Wang, R.K.N.D. Rajapakse, Fuel Cells 15 (2015) 204–213.
[13] C. Lim, L. Ghassemzadeh, F. Van Hove, M. Lauritzen, J. Kolodziej, G.G. Wang, S. Holdcroft, E. Kjeang, J. Power Sources 257 (2014) 102–110.
[14] U.S.Department of Energy Hydrogen Program, Enabling Commercial PEM Fuel Cells with Breakthrough Lifetime Improvements, 2004.
[15] L. Gubler, W.H. Koppenol, J. Electrochem. Soc. 159 (2012) B211.
[16] S. Xiao, H. Zhang, C. Bi, Y. Zhang, Y. Ma, X. Li, H. Zhong, Y. Zhang, J. Power Sources 195 (2010) 8000–8005.
[17] C. Lim, A. Sadeghi Alavijeh, M. Lauritzen, J. Kolodziej, S. Knights, E. Kjeang, ECS Electrochem. Lett. 4 (2015) F29–F31.
[18] M. Zaton, D. Jones, J. Roziere, ECS Trans. 61 (2014) 15–23.
[19] J. Wu, X.Z. Yuan, J.J. Martin, H. Wang, J. Zhang, J. Shen, S. Wu, W. Merida, J. Power Sources 184 (2008) 104–119.
[20] S. Subianto, M. Pica, M. Casciola, P. Cojocaru, L. Merlo, G. Hards, D.J. Jones, J. Power Sources 233 (2013) 216–230.
[21] M.-A. Goulet, R.M.H. Khorasany, C. De Torres, M. Lauritzen, E. Kjeang, G.G. Wang, N. Rajapakse, J. Power Sources 234 (2013) 38–47.
[22] M.-A. Goulet, S. Arbour, M. Lauritzen, E. Kjeang, J. Power Sources 274 (2015) 94–100.
[23] K. Sasaki, M. Shao, R. Adzic, Polymer Electrolyte Fuel Cell Durability, Springer, New York, NY, 2009.
[24] R.M. Darling, J.P. Meyers, J. Electrochem. Soc. 150 (2003) A1523.
[25] K. Asano, Y. Mugikura, T. Watanabe, ECS Trans. 16 (2008) 779–785.
[26] C.A. Reiser, L. Bregoli, T.W. Patterson, J.S. Yi, J.D. Yang, M.L. Perry, T.D. Jarvi, Electrochem. Solid-State Lett. 8 (2005) A273.
[27] W. Gu, R.N. Carter, P.T. Yu, H. Gasteiger, ECS Trans. 11 (2007) 963–973.
[28] S. Kreitmeier, A. Wokaun, F.N. Buchi, J. Electrochem. Soc. 159 (2012) F787–F793.
[29] W. Bi, T.F. Fuller, J. Electrochem. Soc. 155 (2008) B215.
[30] K. Sasaki, F. Takasaki, Z. Noda, S. Hayashi, Y. Shirator, K. Ito, ECS Trans. 33 (2010) 473–482.
[31] J. Zhang, B. Litteer, W. Gu, H. Liu, H. Gasteiger, J. Electrochem. Soc. 154 (2007) B1006.
[32] V. Atrazhev, S.F. Burlatsky, N.E. Cipollini, D.A. Condit, N. Erikhman, ECS Trans. 1 (2006) 239–246.
[33] S.F. Burlatsky, M. Gummalla, V.V. Atrazhev, D.V. Dmitriev, N.Y. Kuzminyh, N.S. Erikhman, J. Electrochem. Soc. 158 (2011) B322.
[34] S. Takaichi, H. Uchida, M. Watanabe, Electrochem. Commun. 9 (2007) 1975–1979.
[35] L. Kim, C.G. Chung, Y.W. Sung, J.S. Chung, ECS Trans. 16 (2008) 945–953.
[36] H. Hagihara, H. Uchida, M. Watanabe, Electrochim. Acta 51 (2006) 3979–3985.
[37] M.J. Eslamibidgoli, P.-É.A. Melchy, M.H. Eikerling, Phys. Chem. Chem. Phys. 17 (2015) 9802–9811.
[38] B. Zhang, D. Wang, Y. Hou, S. Yang, X.H. Yang, J.H. Zhong, J. Liu, H.F. Wang, P. Hu, H.J. Zhao, H.G. Yang, Sci. Rep. 3 (2013) 1836.
[39] Z.Z. Lin, X. Chen, C. Yin, H. Tang, Y.C. Hu, X.J. Ning, Europhys. Lett. 96 (2011) 66005.
[40] T.S. Ahmadi, Z.L. Wang, T.C. Green, A. Henglein, M.A. El-Sayed, Science 272 (1996) 1924–1926.
[41] M. Aoki, H. Uchida, M. Watanabe, Electrochem. Commun. 8 (2006) 1509–1513.
[42] Z. Liu, Y. Yang, W. Lü, C. Wang, M. Chen, Z. Mao, Int. J. Hydrogen Energy 37 (2012) 956–960.
[43] M.P. Rodgers, B.P. Pearman, L.J. Bonville, D. Cullen, N. Mohajeri, D.K. Slattery, J. Electrochem. Soc. 160 (2013) F1123–F1128.
[44] M.P. Rodgers, D.A. Cullen, J. Leonard, D.K. Slattery, J.M. Fenton, in: Carisma 2012 – 3rd Carisma Int. Conf, 2012, pp. 1–19.
[45] S. Helmly, R. Hiesgen, T. Morawietz, X.-Z. Yuan, H. Wang, K. Andreas Friedrich, J. Electrochem. Soc. 160 (2013) F687–F697.
[46] M.P. Rodgers, L.J. Bonville, D.K. Slattery, ECS Trans. 41 (2011) 1461–1469.
[47] S. Helmly, B. Ohnmacht, R. Hiesgen, E. Gülzow, K.A. Friedrich, ECS Trans. 58 (2013) 969–990.
[48] M. Gummalla, V.V. Atrazhev, D. Condit, N. Cipollini, T. Madden, N.Y. Kuzminyh, D. Weiss, S.F. Burlatsky, J. Electrochem. Soc. 157 (2010) B1542.
[49] D. Zhao, B.L. Yi, H.M. Zhang, M. Liu, J. Power Sources 195 (2010) 4606–4612.
[50] N. Ohguri, A.Y. Nosaka, Y. Nosaka, J. Power Sources 195 (2010) 4647–4652.
[51] A. Clark, A. Zhu, K. Sun, H.R. Petty, J. Nanopart. Res. 13 (2011) 5547–5555.
[52] T. Hamasaki, T. Kashiwagi, T. Imada, N. Nakamichi, S. Aramaki, K. Toh,

S. Morisawa, H. Shimakoshi, Y. Hisaeda, S. Shirahata, Langmuir 24 (2008) 7354–7364.
[53] H. Nakanishi, T. Hamasaki, T. Kinjo, K. Teruya, S. Kabayama, S. Shirahata, BMC Proc. 7 (2013) P41.
[54] H. Okamoto, K. Horii, A. Fujisawa, Y. Yamamoto, Exp. Dermatol 21 (2012) 5–7.
[55] K. Hirakawa, S. Sano, Bull. Chem. Soc. Jpn. 82 (2009) 1299–1303.
[56] S. Onizawa, K. Aoshiba, M. Kajita, Y. Miyamoto, A. Nagai, Pulm. Pharmacol. Ther. 22 (2009) 340–349.
[57] N. Macauley, L. Ghassemzadeh, C. Lim, M. Watson, J. Kolodziej, M. Lauritzen, S. Holdcroft, E. Kjeang, ECS Electrochem. Lett. 2 (2013) F33–F35.
[58] N. Macauley, A. Sadeghi Alavijeh, M. Watson, J. Kolodziej, M. Lauritzen, S. Knights, G. Wang, E. Kjeang, J. Electrochem. Soc. 162 (2015) F98–F107.
[59] Y. Shiraishi, M. Hashimura, M. Nakao, T. Ishizu, M. Kazita, Y. Miyamoto, N. Toshima, Supramol. Chem. 23 (2011) 195–198.
[60] P.-C. Chen, G. Liu, Y. Zhou, K.A. Brown, N. Chernyak, J.L. Hedrick, S. He, Z. Xie, Q.-Y. Lin, V.P. Dravid, S.A. O'Neill-Slawecki, C.A. Mirkin, J. Am. Chem. Soc. 137 (2015) 9167–9173.
[61] G. Liu, D.J. Eichelsdoerfer, B. Rasin, Y. Zhou, K.A. Brown, X. Liao, C.A. Mirkin, Proc. Natl. Acad. Sci. U. S. A. 110 (2013) 887–891.
[62] Y. Zhou, X. Zhou, D.J. Park, K. Torabi, K.A. Brown, M.R. Jones, C. Zhang, G.C. Schatz, C.A. Mirkin, Nano Lett. 14 (2014) 2157–2161.
[63] C. Gu, H. Xu, M. Park, C. Shannon, ECS Trans. ECS (2008) 181–190.
[64] C. Gu, H. Xu, M. Park, C. Shannon, Langmuir 25 (2009) 410–414.
[65] S.B. Simonsen, I. Chorkendorff, S. Dahl, M. Skoglundh, J. Sehested, S. Helveg, J. Am. Chem. Soc. 132 (2010) 7968–7975.
[66] A.P. Young, J. Stumper, S. Knights, E. Gyenge, J. Electrochem. Soc. 157 (2010) B425.
[67] M. Nesselberger, S. Ashton, J.C. Meier, I. Katsounaros, K.J.J. Mayrhofer, M. Arenz, J. Am. Chem. Soc. 133 (2011) 17428–17433.
[68] L. Wang, Y. Yusuke, J. Am. Chem. Soc. 131 (2009) 9152–9153.
[69] P.J. Ferreira, Y. Shao-Horn, Electrochem. Solid-State Lett. 10 (2007) B60.
[70] E. Ben-Jacob, R. Godbey, N.D. Goldenfeld, J. Koplik, H. Levine, T. Mueller, L.M. Sander, Phys. Rev. Lett. 55 (1985) 1315–1318.
[71] M.A. Mahmoud, C.E. Tabor, M.A. El-Sayed, Y. Ding, Z.L. Wang, J. Am. Chem. Soc. 130 (2008) 4590–4591.
[72] D.-H. Kwak, Y.-W. Lee, K.-H. Lee, A.-R. Park, J.-S. Moon, K.-W. Park, Int. J. Electrochem. Sci. 8 (2013) 5102–5107.
[73] C.-Y. Chiu, Y. Li, L. Ruan, X. Ye, C.B. Murray, Y. Huang, Nat. Chem. 3 (2011) 393–399.
[74] K.H. Wong, E. Kjeang, J. Electrochem. Soc. 161 (2014) F823–F832.
[75] H. Uchida, Y. Ueno, H. Hagihara, M. Watanabe, J. Electrochem. Soc. 150 (2003) A57–A62.